Full Length Article

Microstructured plastic scintillators for pencil beam profiling in proton-therapy accelerators

Veronica Leccese [a], Michele Caldara [a,*], Samuele Bisi [a], Marcello Pagano [a], Simone Gargiulo [a], Carlotta Trigila [b], Arnaud Bertsch [c], Alessandro Mapelli [d,e], Fabrizio Carbone [a]

[a] *Institute of Physics (IPhys), Laboratory for Ultrafast Microscopy and Electron Scattering (LUMES), École Polytechnique Fédérale de Lausanne (EPFL), Lausanne 1015 CH, Switzerland*
[b] *Department of Biomedical Engineering, University of California, Davis, Davis, CA, United States*
[c] *Institute of Electrical and Micro Engineering (IEM), Laboratory of Microsystems (LMIS4), École Polytechnique Fédérale de Lausanne (EPFL), Lausanne 1015 CH, Switzerland*
[d] *Institute of Mechanical Engineering (IGM), Advanced NEMS Laboratory (NEMS), École Polytechnique Fédérale de Lausanne (EPFL), Lausanne 1015 CH, Switzerland*
[e] *Confovis GmbH, Jena, Germany*

ARTICLE INFO

ABSTRACT

A novel beam profiler based on microstructured scintillation resin is presented. The detector consists of a bundle of waveguides, featuring an active area of 30×30 mm^2 with a fill factor of 50% and a pitch of 400 μm. This configuration is obtained by casting a scintillating resin into a microfabricated Polydimethylsiloxane (PDMS) mold. A prototype, coupled to an array of photodiodes and readout electronics, potentially allowing profile rates up to 7 kHz, has undergone testing with an ultraviolet (UV) source and a proton beam accelerated at different energies, typical of those employed in proton therapy. The experimental results obtained during the test campaigns were compared with theoretical simulations demonstrating a good agreement with the modeling expectations, thus confirming the validity of this novel design for microstructured scintillating detectors.

1. Introduction

The number of proton therapy (PT) facilities in the world is growing at a fast rate, with more than 110 centers in operation at this time and approximately 60 centers under construction or planning (https://ptcog.site/). A large part of the PT centers have more than one treatment room or a gantry, which implies having high-energy beam transfer lines several meters long and rather complex layouts [1–4]. In this scenario, beam instrumentation and diagnostics play a key role, especially during the commissioning of a new accelerator and, once a facility is in operation, during the machine quality assurance (QA). In the latter case, beam measurements can reveal subtle drifts or deviations from reference settings, allowing beam physicists to maximize the accelerator up-time, which typically needs to be higher than 97% in a medical facility. Nowadays, modern PT centers use pencil beams, i.e. beams with small transverse dimensions, which can scan tumor slices to reach unprecedented dose conformity and precision [5].

One of the beam parameters that needs to be regularly monitored is the beam transverse profile, which knowledge is necessary to set the correct optics in the accelerator and, in conjunction with quadrupoles and dipoles, it is used to measure the beam emittance, energy, and energy spread [6].

Over the past decades, various solutions have been proposed and refined to measure beam transverse profiles in the horizontal and vertical planes. These include wire-based technologies such as profile grids or wire scanners [7,8], gas-ionization-based devices like residual gas monitors [9], and scintillating material-based devices like scintillating screens or fibers [10]. Recently, scintillating fibers and plastic scintillators connected to photodetectors and readout systems have emerged as a simple and reliable solution for beam diagnostics [11–13]. However, these detectors are not without their drawbacks, notably a limited lifetime due to permanent radiation damage on the fibers most exposed to the beam [14], and spatial resolution constrained by the dimensions of the fibers (smallest commercial scintillating fibers have dimension of 200 μm [15]). Furthermore, the assembly of numerous fibers with precise alignment is a laborious and complex process, especially when covering a large area.

As an alternative to scintillating fibers assemblies, microchannels filled with scintillating liquid have been proposed [16–19]. However,

---

* Corresponding author.
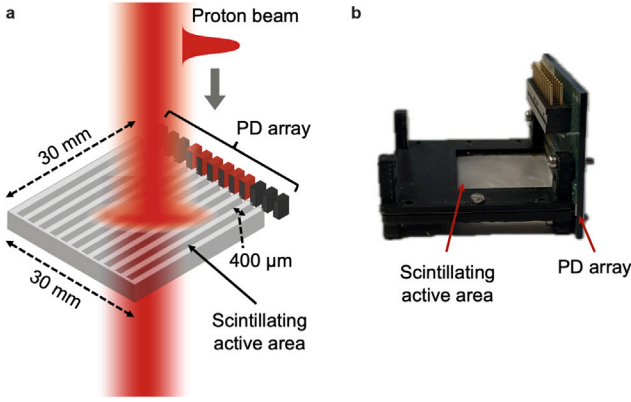 *E-mail address:* michele.caldara@epfl.ch (M. Caldara).

Fig. 1. (a) Schematic illustration of the microstructured plastic scintillator. (b) Picture of the actual device, comprising the active area, the PD array, and the support frame.

Fig. 2. Simulated profiles computed at the PDs position (blue lines), compared with the horizontal profile of the proton source (red dashed line).

challenges related to the homogeneous filling of microchannels and the risk of liquid leaks make these devices less suitable for high vacuum applications. Recently, a complementary metal–oxide–semiconductor (CMOS) detector demonstrated success operating in air, monitoring a pencil proton beam scanned source, representing a promising alternative for beam transverse profile monitoring [20]. Notably, for minimally invasive detectors, particularly relevant for circular accelerators, substantial progress has been reported on residual gas [9] or gas curtain [21] devices.

In this context, we present a microfabricated scintillating resin-based detector designed to achieve approximately 115 μm - spatial resolution and overcome radiation damage issues. This device, intended for transverse profile monitoring in particle accelerators, is meant to address the limitations associated with existing beam profilers.

2. Microscintillator-based beam profiler

The operational mechanism of the microscintillator-based beam profiler relies on the detection of photons resulting from the scintillation upon the impact of a particle beam on the active area of the instrument. The active area comprises 75 channels, each featuring a square cross-section of 200 μm × 200 μm and a length of 30 mm. The channel's pitch length is 400 μm. The overall active area of the device is 30×30 mm^2 with a fill factor of 50%. This configuration is compatible with the typical beam transverse dimensions in most diffused PT accelerators [22]. The 400 μm pitch allows achieving a theoretical resolution of approximately 115 μm, which can be further reduced by decreasing the pitch size [23,24]. Due to the different refractive indices of the scintillating resin ($R = 1.58$) and the surrounding air/vacuum, the channels function as a waveguide for photons, guiding them as long as they strike the resin-air interface with an angle smaller than the critical one (39.2°). These guided photons are directed toward an array of photodetectors (PDs) spaced between them with the same pitch as the microchannels. The PDs detect and convert the photons into a sequence of electrical signals that are elaborated by a microcontroller on a custom-made printed circuit board (PCB). By knowing the geometry of the PDs and the amplitude of each photodiode signal, the beam transverse profile is obtained.

In Fig. 1(a) a schematic representation of the device is presented, while Fig. 1(b) shows a picture of the actual device. The active area is supported by a plastic frame, accommodating the photodetector (PD) array.

2.1. Modeling and simulations

The device has been modeled using GATE (v 9.1) [25–28], an open-access Monte-Carlo simulation software dedicated to medical imaging
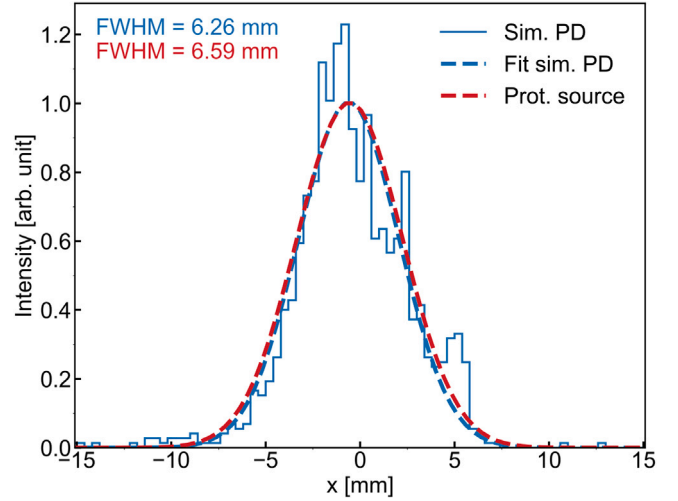
and radiotherapy, based on the GEANT4 toolkit [29]. The backbone code used for our simulations has been retrieved from LUT Davis Model [30, 31], modified to include proton-matter interaction, the waveguides geometry, and the material properties discussed above. The simulations account for the generation of photons from a proton beam, their transport within the channels, and their final interaction with the air. Each simulation generates two data frames: 'Hits' and 'Phase space'. The 'Hits' data frame contains the position and the direction of each photon, while the 'Phase space' is a user-defined surface where the position and the direction of the outgoing particles (both protons and photons) are recorded. To enable a meaningful comparison with the experimental results, the simulated proton beam is configured with a Gaussian distribution mirroring the parameters used in the experimental tests. The simulated protons have an energy of 300 mm Water Equivalent Thickness (WET) (218 MeV), with a full-width half maximum (FWHM) of 7.72 mm. The direction and position of the beam are set to impinge perpendicularly on the center of the active area.

Fig. 2 shows the comparison between the simulated profile at the PDs and the input proton beam profile. The two profiles are in good accordance, indicating an error of 5% in the FWHM. The non-Gaussian distortions observed in the simulated profile are primarily attributed to the reduced statistical significance resulting from a limited number of simulated particles (N = 100).

The prototype described in this paper exhibits an air gap of 1 mm between the end of the channels and the PD array. The air gap was added in the mechanical holder design as a margin to avoid the PDs touching the active area, considering also that the holder is 3D-printed in Polylactide (PLA). To quantify the effect of the air gap on the measured profile, we simulated a point-like proton source impinging at the midpoint of the sole central channel and having a transverse distribution that completely fits in one channel width (FWHM of 141 μm).

The results, reported in Fig. 3, reveal that in the absence of an air gap, all the photons are collected by the PD in front of the central channel. Conversely, introducing a 1 mm air interface broadens the distribution of the detected photons (FWHM ~ 1.90 mm) causing a response from neighboring PDs as well, and reduces by a factor of 10 the number of photons collected by the PD in correspondence of the central channel.

Thanks to the simulation model, it is possible to estimate the beam profiler detection efficiency η by taking into account different contributions:

$$\eta = \eta_{Scint} \cdot \eta_{Waveguide} \cdot \eta_{Air} \cdot \eta_{PD} \tag{1}$$
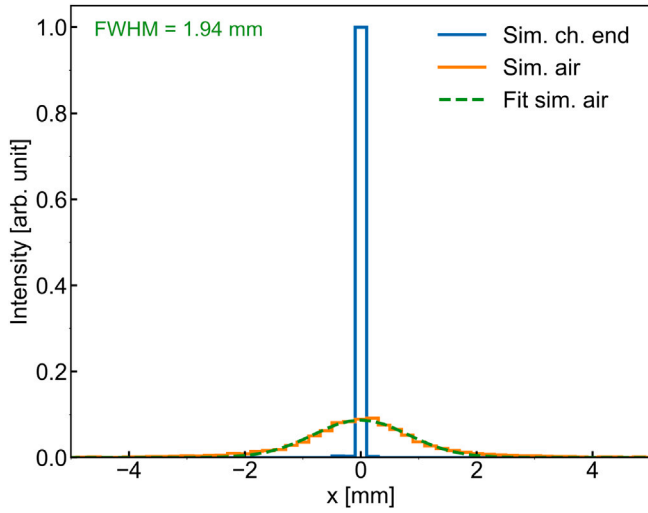
Fig. 3. Simulated profiles at the end of the channels (blue line) and after 1 mm of air (orange line), obtained using a source featuring an FWHM = 141 μm impinging on the central channel.

Fig. 4. Main steps of the fabrication process: (a) channels etching into a silicon wafer, (b) PDMS mold made using the silicon master, (c) pouring of the scintillating resin into the PDMS mold, (d) the final active area made in resin is a replica of the silicon master.

where $\eta_{Scint} = \frac{n_{sim}}{n_{exp}}$ is the ratio between the total number of simulated scintillation photons and those expected, computed as $n_{exp} = Y \cdot E_{dep}$. Y is the scintillation yield of the selected resin (9000 photons/MeV from its datasheet), and E_{dep}, which depends on the impinging beam energy and intensity, is the energy deposited by protons in the thickness of the scintillator (200 μm), computed according to the Bethe–Bloch formula [32]. $\eta_{Waveguide}$ takes into account the transport efficiency of the photons inside the channels and it is computed as the ratio between the photons arriving at the end of the channels, at the PDs side, and the total number of photons generated by scintillation. η_{Air} takes into account the effects of the air gap between the channel end and the PDs, and it is given by the number of photons collected by all the PDs over the number of those exiting the end of the individual channel. Finally, η_{PD} is the quantum efficiency of the PD, defined as $\eta_{PD} = \frac{E \cdot R}{e}$, where E is the photon energy, R the PD responsivity, *i.e.*, the ratio between the photocurrent and the incident optical power, and e is the charge of the electron. In the examined case of a proton beam with an energy of 300 mm WET (218 MeV), $\eta_{Scint} = 0.49$, which represents the 50% filling factor of the scintillator on the detector active area. Concerning the other efficiency contributions, $\eta_{Waveguide} = 0.16$ and $\eta_{Air} = 0.20$. η_{Air} would increase up to 1 if the PDs were in contact with the end of the waveguides. At the simulated energy of 300 mm WET (218 MeV), around 12 photons per proton would reach the PDs. $\eta_{PD} = 0.59$ for photon energy of 423 nm, which is the peak emission of the scintillating resin used to fabricate the detector's active area. Thus, the total efficiency amounts to $\approx 0.9\%$.

2.2. Microfabrication process

The scintillating microchannels have been prepared starting from silicon masters patterned with microchannels having a width of 200 μm and a pitch of 400 μm. We fabricated silicon masters by standard microfabrication techniques, *i.e.*, optical lithography for patterning the channels, followed by deep reactive ion etching (DRIE) (see Fig. 4a). After the DRIE, silicon walls feature a typical undulation, known as the 'scalloping effect', which is due to a slight in-plane etching of silicon. To remove the scalloping effect, a layer of 2 μm of silicon oxide was grown on the etched channels and etched afterward by buffered hydrofluoric acid (BHF) [19]. Having smooth walls (surface roughness smaller than the photon wavelength) is desirable to maximize photon transmission along the waveguides towards the PDs.
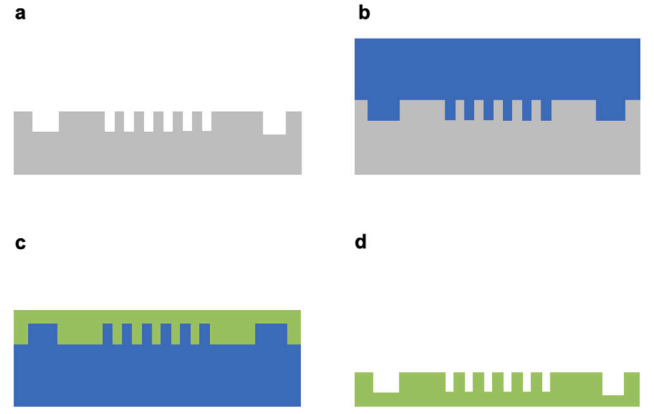
The silicon masters were used to make Polydimethylsiloxane (PDMS) molds (see Fig. 4b). The pattern on the silicon master was replicated with high accuracy (roughness better than 400 nm) on PDMS molds (see Fig. 5a), which were filled with the scintillating resin thereafter (see Fig. 4c). The final active area made in resin is a replica of the original silicon master (see Fig. 4d). The resin (EJ-290 by Eljen Technology) is composed of three parts. Part A contains a partially polymerized plastic scintillator, *i.e.*, oligomers of Vinyl Toluene (VT). Part B is composed of VT monomers, 2,5- Diphenyloxazole (PPO), 1,4-Bis(5-phenyl-2-oxyzole) benzene (POPOP), and 2,6-Dit-tert- butyl-p-cresol (DBPC). PPO and POPOP are the primary and secondary fluorophores operating as wave shifters. The wave shifters are used to convert the non-radiative ionization radiation produced by Polyvinyl Toluene to lower energy photons (blue or green) that are detectable with the PDs array. Part C contains Lauroyl peroxide, a thermal initiator, added for VT polymerization and cross-linking.

The resin is viscous before polymerization, which takes approximately 3 h at 80 °C. Once it is polymerized, the detector can be demolded from the PDMS mold: the result is a self-standing scintillating area patterned as the original silicon master. To facilitate the demolding process, a surface treatment was performed on the polymeric molds. It consists of exposing the mold to the oxygen plasma, followed by a silane (Perfluorooctyltriethoxysilane, PFTOS) coating deposited in the gas phase. Fig. 5b shows the beam profiler active area after the demolding; it is worth noting that a residual thin layer of resin keeps the channels together. The metrology of the devices has been performed with a Scanning Electron Microscope (SEM) (see Fig. 5c) and an optical profilometer (see Fig. 5d), which confirms the depth of the channels to be $\sim 211 \pm 1$ μm. Although repeatable, this value is 5.5% larger than the desired depth (200 μm), because of the settings of the dry etcher machine necessary for the silicon master fabrication step (etching rate, time, accuracy). In contrast to depth, the width and pitch of the channels are dictated by the silicon master photolithography, thus they respected the design values with an accuracy better than 1 μm. The thickness of the residual thin layer was measured to be ~ 80 μm. A more detailed description of the fabrication process is reported in the Supplementary Information.

The main advantage of this fabrication method is the possibility to obtain geometrically accurate and low-cost detectors, whose active area can be easily replaced if a degradation due to radiation damage occurs. In addition, the achievable beam profile resolution is higher than the standard scintillating fiber-based detectors currently used for beam diagnostics and experiments.
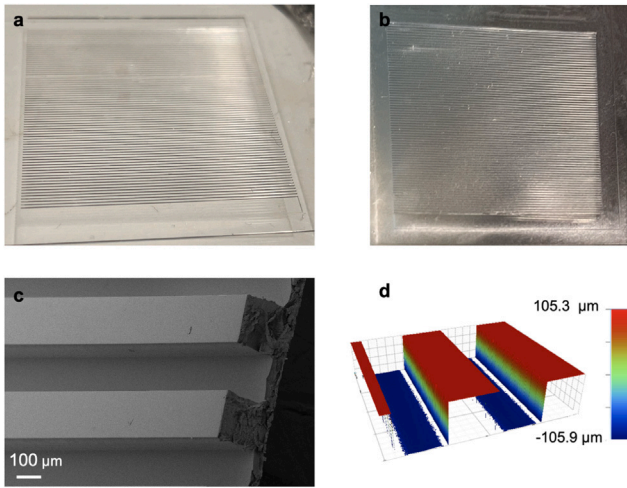
Fig. 5. (a) PDMS mold realized using a silicon master patterned with 200 μm-width channels. (b) Microchannels made by scintillating resin, obtained by demolding the resin from PDMS molds, after a PFTOS surface treatment. (c) and (d) Scanning Electron Microscope (SEM) image and 3D measurement of the resin active area geometry taken by an optical profilometer, showing smooth vertical walls and a very accurate reproduction of the PDMS mold.

2.3. Readout and control

2.3.1. Photodiode array

The scintillating light exiting each detector channel needs to be carefully converted into an electronic signal to obtain an accurate profile. For this purpose, a linear array of 128 photodiodes with integrated amplifiers has been chosen (S13885-128, Hamamatsu). In particular, the PDs pitch is 400 μm, while each PD is 300 μm wide and 600 μm high. Moreover, the PDs work in an extended visible spectral range from 200 nm to 1000 nm, with a peak sensitivity at $\lambda = 720$ nm. At the wavelength of the peak of the scintillation process (423 nm), the approximate PD sensitivity is 0.26 A/W.

One of the biggest advantages of using commercial PD arrays is the presence on board of an integrated charge amplifier array followed by a clamp and hold circuit, allowing a serial output and a relatively simple digital interface, consisting of only a clock (CLK) and a line aimed to set the desired integration time of the charge integrators connected to each PD. The achievable profile rate, which depends on the CLK frequency f_{CLK} and on the number of PD N_{PD}, is expressed in the Eq. (2).

$$f_{Profile} \leq f_{CLK}/(16.5 + 4 \cdot N_{PD}) \tag{2}$$

Considering that the maximum allowed clock frequency is 4 MHz, the maximum profile rate can be as high as 7568 Hz, which is considerably higher than commonly used scientific cameras and largely fulfills the typical needs of a beam profiler in a DC or pulsed particle therapy accelerator; The minimum integration time can be as low as 4.5 μs if the maximum CLK frequency of 4 MHz is used. The maximum integration time is limited by the saturation of the PD analog output. The dark state output voltage is typically 2.5 V (normally high) and the PDs, when illuminated, generate a train of inverted pulses whose amplitude is proportional to the integrated light. The voltage of each PD output can go as low as 0.7 V when it reaches saturation. The photoresponse non-uniformity declared by the manufacturer can be as high as ±10%, which would directly translate into a profile deformation. For this reason, an online calibration tool using UV light has been developed.

The PD array is mounted on a G10 glass-epoxy printed circuit board (PCB). The electronics and the wire bonds are protected with resin. The PCB presents four 2.2 mm diameter mounting holes precisely machined with respect to the position of the PD array. Since the declared mechanical tolerances is of the order of ±0.2 mm, an accurate alignment

procedure with a microscope had to be put in place during the assembly of the PD array with the detector in order to position the center of the PDs in correspondence with the center of the waveguides outputs and thus maximize the collection of the photons from scintillation.

2.3.2. Controller

The second electronic block of the system is a controller with twofold functions: (i) to generate all needed supply voltages for the PD array and (ii) to provide the analog and digital interface to it. The core of the custom-developed board is a programmable microcontroller module (MCU, Nucleo-G431KB, STMicroelectronics), which is powered by a standard 5 V micro-USB cable. The Nucleo board generates a 3.3 V (max 500 mA) which is used to power the PD array. For what concerns the 2.5 V needed for the analog circuitry of the PD array integrated circuit, a low noise low dropout regulator is used (LP5907, Texas Instruments). The analog signal V_{Out} from the PD array is buffered and takes two parallel paths: the MCU analog input and a coaxial subminiature version A (SMA) connector for acquisition into another system. The MCU includes an analog-to-digital converter (ADC) of 12 bits capable of reaching a sample rate of 4 MHz and presenting also an external trigger capability, using the trigger signal coming from the PD array. The clock and the integration timeline are programmable via the MCU firmware, allowing for a maximum flexibility according to the measurements needed. The controller PCB presents also an external trigger connector, such to measure a beam profile synchronous with an experiment event. Finally, the serial interface peripheral of the MCU is connected to the PCB to program a data transfer across a field cable if necessary.

2.3.3. UV-Light Emission Diodes calibration tool

An additional PCB has been developed with the main purpose of illuminating the detector's active area with UV-C light. Despite this kind of source is not able to generate true scintillation in the material, it is absorbed by the fluors of the scintillator, which re-emit the light in the visible range. This method turned out to be a convenient tool to determine the overall detector yield, which is a combination of active area fabrication imperfections, detector-PD array misalignment, and PD array non-uniformity. Moreover, as suggested in [14], UV light might help in the radiation damage recovery process of the scintillator. Two Light Emission Diodes (LEDs), spaced by 15 mm and pointing to the active area at its periphery, emit narrow UV-C radiation with a peak wavelength at 273 nm (model VLMU35CB2-275-120, Vishay); the emitted UV light reaches the detector thanks to the LED angle of the half intensity of ±60°. Fig. 6 shows the theoretical Lambertian emission of one single LED in a polar plot and the computed luminous intensity resulting at the detector surface in correspondence to the LEDs, in the case when both LEDs are lit. The obtained experimental profile, despite revealing some detector non-uniformity and asymmetries due to misalignment, follows the theoretical curve.

3. Experimental validation

The beam profiler prototype has been tested on a proton beam at the National Centre for Oncological Hadrontherapy (CNAO) in Pavia, Italy [2]. Each of the three available treatment rooms at CNAO can deliver to patients protons with an energy ranging from 33 mm WET (62.7 MeV) to 326 mm WET (228.6 MeV) [33]. The beam FWHM at the isocenter varies as a function of energy from 22 mm to 7 mm in both transverse planes. In the performed experiments the protons were delivered to the isocenter as a non-scanning beam on their nominal trajectory and, after traversing the device under test, they were dumped in a water tank. In each beam extraction, lasting typically 1 s, up to $3 \cdot 10^9$ protons can be directed to the patient. Each treatment room is equipped with a Dose Delivery System (DDS), capable of monitoring and controlling the beam delivery according to the treatment plan. In particular, at CNAO, the required beam charge is constantly monitored
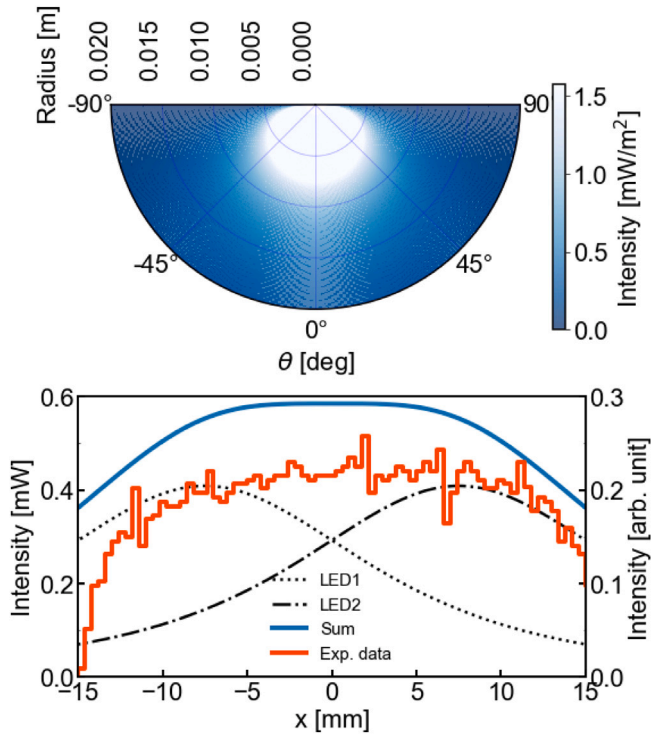
Fig. 6. Lambertian emission of the UV Led using an emitted power of 2.6 mW at $I_f = 20$ mA (Top) and comparison between the theoretical luminous intensity at the detector surface with both LEDs lit and the experimental profile (Bottom).

Fig. 7. Treatment room at CNAO. The red arrow indicates the device, which is placed on the patient's bed ~ 55 cm from the isocenter. The white boxes at the end of the bed are full of water and are meant to stop the beam. The two reference detectors (DDS and ISO) are also marked.

and the beam being extracted from the synchrotron is interrupted when the desired charge is delivered in the treatment room at a given energy. During the experiments, the charge was set to that of $5 \cdot 10^8$ protons. The DDS is composed of a strip ionization chamber with a strip pitch of 1.65 mm, plus an integral plane ionization chamber to monitor the charge. In the results presented in this section, an additional set of reference profiles at the isocenter (ISO) has been also considered. Those data were taken before the experiment with a dedicated ionization chamber with a strip pitch of 1 mm. The DDS is permanently installed 87.35 cm upstream of the isocenter, in the air, just after a vacuum window. Our prototype has been installed on the patient bed approximately 55 cm downstream of the isocenter, on a support stand (see Fig. 7). Due to the limited time available and the mechanical setup, only the vertical transverse plane was measured. Repeatability was verified measuring beam profiles during at least five beam extractions for each chosen beam energy. The profile measurements were triggered using the timing signal of extraction start and the controller was programmed to set 10 ms integration time for the PDs. The PDs serial analog output was acquired on an oscilloscope and saved locally for post-processed in Python. The oscilloscope was controlled remotely from the medical treatment room, so as to be able to have real-time visual feedback on the measurements. The detector successfully measured its first proton profiles, demonstrating a high sensitivity. In fact, for proton energies lower than 141 mm WET (142 MeV) the measured profiles saturated. The profiles were visible until the highest tested energy of 300 mm WET (218 MeV). Since the typical extraction lasts 1 s and the charge was fixed at $5 \cdot 10^8$ protons, we can deduce that the beam profiler was integrating signal generated by approximately $5 \cdot 10^6$ protons.

The beam spot center of mass (COM) and standard deviation as a function of energy have been calculated by processing the acquired profiles and they are shown in Fig. 8 together with the results from the reference profiles obtained at the DDS and the ISO. For what concerns data processing, since the profiles might present tails or some pedestal that can heavily affect the computation of the center of mass and

beam transverse size, the raw profile amplitudes have been zeroed for values below 5% of the maximum before being fitted with a Gaussian to extract the COM and standard deviation. It can be noted that, while the COM is relatively constant at various energies, the beam size increases from DDS to the ISO due to the Multiple Coulomb Scattering (MCS) through the vacuum window, the DDS material, and the path in the air. Moreover, as expected, the beam spot widening is more pronounced for low energies. The COM measured with our device differs by 700 μm from the reference ones, which can be explained by the manual alignment, which was made only using two orthogonal lasers indicating the x-y and y-z planes (axes shown in Fig. 7). The beam transverse size measured by our detector was systematically much larger than expected. Computing the contribution of the MCS using Highland [34] approximation, the beam transverse sigma should increase only between 70 and 30 μm from low to high energy with respect to that shown in Fig. 8 at ISO. Thus the beam profile is indeed broadened by additional fabrication and geometrical factors, as discussed in the next section.

4. Discussion

The geometry of the real detector was implemented in the simulation model to quantify the contribution of the 80 μm thick residual layer of scintillating material that binds together the microfabricated waveguides and the 1 mm air gap between the waveguides end and the PDs, to study the profile-broadening effect appeared during the experiment at CNAO. Fig. 9 shows on the same plot the newly simulated profile together with the reference (CNAO ISO) and the measured one. The simulation reveals an FWHM $\sim 35\%$ larger than the reference. However, the simulation cannot fully explain the widening of the experimental profile, which is still $\sim 44\%$ broader than the simulated one. This could be due to factors such as the roughness and defects at the channel end's surface, the vertical alignment between the waveguides and the photodiodes, and a too-large air gap. In terms of overall detector efficiency, using the beam properties and the detector geometry of Fig. 9, we computed and simulated the different efficiency contributions introduced in Section 2.1. Due to the presence of a residual thin layer of resin, the η_{Scint} was 0.6 as compared to 0.49 with no layer, while $\eta_{Waveguide}$ did not change. The resulting total efficiency amounts to 1.13%. Considering the computed 12 photons per proton able to reach the PDs (see Section 2.1), the estimated $5 \cdot 10^6$ protons used to measure a profile and the updated total efficiency, around $73.5 \cdot 10^6$ photons were captured by the PDs to obtain the profile shown in Fig. 9.
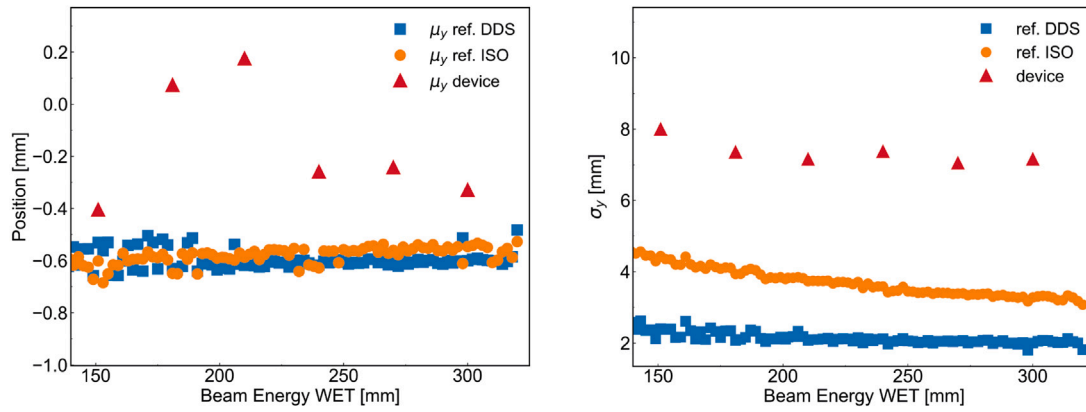
Fig. 8. Summary of the experimental results on CNAO proton beams for six different energies, in the vertical plane. Left: COM (μ_y) of the beam profiles. Right: beam transverse profile standard deviation (σ_y). The results obtained with the profiler device are shown together with the reference data from CNAO DDS and ISO ionization chambers. Proton energy is represented in Water Equivalent Thickness (WET).
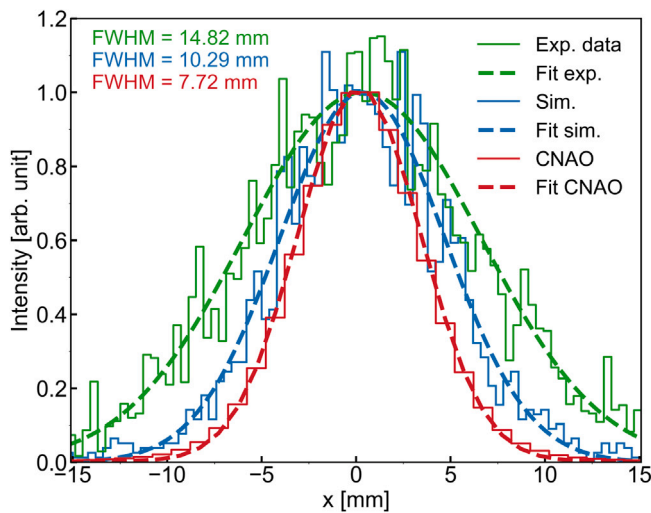

Fig. 9. Simulated profile of the detector with residual resin layer (blue), compared with the experimental (green) and the reference one at ISO (red) for a proton beam at 300 mm WET (218 MeV).

Fig. 10. Simulated beam profiles obtained from a point-like source with an FWHM of 141 μm and a detector including the thin residual layer linking all waveguides and PDs at 1 mm from channels end. Photon distributions are shown at the channel end (blue line) and at the PDs (orange line).

To further investigate the effect shown in Fig. 9, the same point-like proton source of Fig. 3, impinging on the midpoint of the central channel of the device, was used in a simulation with the detector presenting the residual layer and with PDs at 1 mm distance from the channels end. As shown in Fig. 10, the presence of the excess layer of resin spreads laterally the photons, originally generated in the sole central waveguide, across a region of ± 5 mm. The photon distribution looks slightly wider and smoothed plotting the simulation results at the PDs, due to the effect of the 1 mm air gap. From the results above, it is clear that the residual scintillating resin layer is the main contributor to the profile widening. In fact, without it, the simulated photons' cross-talk is only due to the air gap, which spreads the photons on a region of ± 2 mm around the stimulated channel (see Fig. 11). However, the excess resin layer serves as a mechanical support for the waveguides and it is necessary to maintain the whole structure together.

The beam profiler prototype presented in this paper presents some interesting advantages as the accuracy of the microfabricated active area and its high sensitivity; the resin structure, which can potentially be produced in small series from the same PDMS mold, could be replaced when degradation due to ionizing radiation appears. The electronics and readout allow to set programmable integration times, read profiles at a high rate, and characterize the response of the detector by UV LEDs illumination. However, the fabrication and the experimental
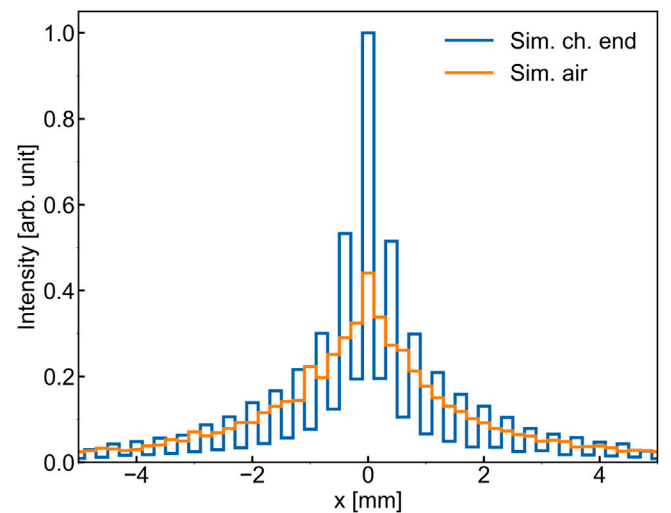
characterization revealed some weaknesses, as the broadening effect of the beam profile mainly due to the residual resin layer and the difficult alignment between the waveguides and the PDs. The PDs array with integrated amplifiers, despite being a few mm from the beam, did not show any malfunction during the experiment, but more beam time will be needed to further investigate its behavior.

5. Conclusion

In this work, we presented the development of a novel beam profiler obtained by casting scintillating resin on a microfabricated structure obtained from a silicon master device. The proof of concept detector covers an area of 30 × 30 mm^2 with an array of square section scintillating waveguides of 200 μm spaced by 400 μm. The active area is mechanically self-sustaining and it exploits the surrounding air/vacuum refractive index to guide the scintillating photons along its channels to a photodiode array and a controller card, where one-shot profiles can be measured at a rate as high as 7 kHz. A prototype assembly of the detector, holder, and readout electronics was used first under UV illumination and measured successfully its first profiles on a real proton beam used for therapy at CNAO. The preliminary measurements presented in this work showed great sensitivity across
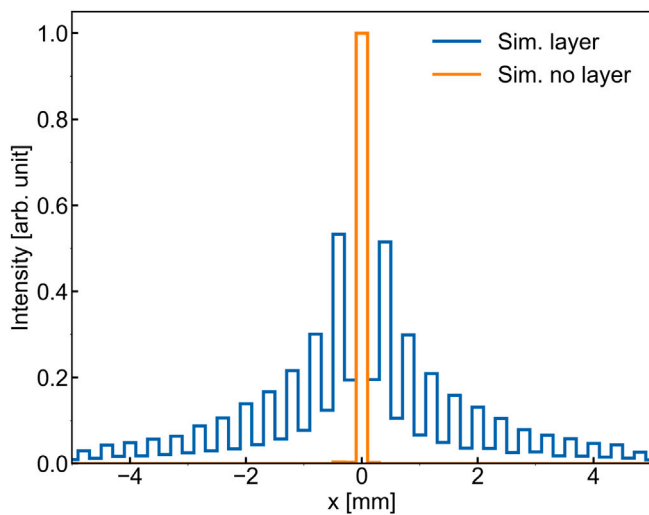
Fig. 11. Comparison between simulated photons distributions at channels end of a device with (blue line) and without (orange line) the thin residual resin layer. Point-like beam with an FWHM of 141 µm impinging on the central channel.

all energy ranges (33–326 mm WET, corresponding to the range 62.7–228.6 MeV); only 5 million protons were used at 6 different beam energies to obtain the profiles. However, the thin layer of resin linking all channels and the air gap between the channel ends and the PDs contribute to an unwanted profile broadening. This effect should be addressed in the next fabrication iterations. Future activities will also focus on the coupling between the active area and the PD array, the demolding process, and the surface quality of the channel extremities. Moreover, the detector is currently being built with double resolution (pitch 200 µm) and improved mechanical properties. In conclusion, the profiler prototype presented in this paper, if further developed into an in-vacuum, motorized instrument, potentially represents a flexible and accurate beam diagnostics tool for proton or heavy ion medical accelerators, especially those generating pencil beams.

CRediT authorship contribution statement

Veronica Leccese: Conceptualization, Data curation, Formal analysis, Investigation, Methodology, Writing – original draft, Writing – review & editing. **Michele Caldara:** Conceptualization, Data curation, Formal analysis, Investigation, Methodology, Software, Validation, Visualization, Writing – original draft, Writing – review & editing. **Samuele Bisi:** Data curation, Formal analysis, Software, Writing – original draft. **Marcello Pagano:** Investigation, Methodology. **Simone Gargiulo:** Formal analysis, Software. **Carlotta Trigila:** Software. **Arnaud Bertsch:** Investigation, Methodology, Writing – review & editing. **Alessandro Mapelli:** Conceptualization, Investigation, Methodology, Writing – review & editing. **Fabrizio Carbone:** Conceptualization, Funding acquisition, Project administration, Resources, Supervision, Validation, Visualization, Writing – review & editing.

Declaration of competing interest

The authors declare the following financial interests/personal relationships which may be considered as potential competing interests: Michele Caldara reports financial support was provided by ADAM SA. Michele Caldara reports a relationship with ADAM SA that includes: employment. Veronica Leccese, Michele Caldara, Marcello Pagano, Arnaud Bertsch, Alessandro Mapelli, Fabrizio Carbone has patent #P3695US00 pending to EPFL.

Appendix A. Supplementary data

Supplementary material related to this article can be found online at https://doi.org/10.1016/j.nima.2024.169176.

References

[1] A. Koschik, et al., Gantry 3: Further development of the PSI PROSCAN proton therapy facility, in: Proc. 6th International Particle Accelerator Conference (IPAC'15), Richmond, VA, USA, May 3-8, 2015, in: International Particle Accelerator Conference, (6) JACoW, Geneva, Switzerland, 2015, pp. 2275–2277, http://dx.doi.org/10.18429/JACoW-IPAC2015-TUPWI016, URL http://jacow.org/ipac2015/papers/tupwi016.pdf.

[2] S. Rossi, The national centre for oncological hadrontherapy (CNAO): Status and perspectives, Phys. Med. 31 (4) (2015) 333–351, http://dx.doi.org/10.1016/j.ejmp.2015.03.001, URL https://www.sciencedirect.com/science/article/pii/S1120179715000617.

[3] A. Peters, R. Cee, E. Feldmeier, M. Galonska, T. Haberer, K. Höppner, M. Ripert, S. Scheloske, C. Schoemers, T. Winkelmann, et al., Operational status and further enhancements of the HIT accelerator facility, IPAC 10 (2010) 73.

[4] F. Ulrich-Pur, L. Adler, T. Bergauer, A. Burker, A. De Franco, G. Guidoboni, A. Hirtl, C. Irmler, S. Kaser, S. Nowak, F. Pitters, M. Pivi, D. Prokopovich, C. Schmitzer, A. Wastl, Commissioning of low particle flux for proton beams at MedAustron, Nucl. Instrum. Methods Phys. Res. A 1010 (2021) 165570, http://dx.doi.org/10.1016/j.nima.2021.165570, URL https://www.sciencedirect.com/science/article/pii/S0168900221005556.

[5] M. Durante, R. Orecchia, J. Loeffler, Charged-particle therapy in cancer: clinical uses and future perspectives, Nat. Rev. Clin. Oncol. 4 (2017) 483–495, http://dx.doi.org/10.1038/nrclinonc.2017.30.

[6] P. Strehl, Beam Instrumentation and Diagnostics, 2006, http://dx.doi.org/10.1007/3-540-26404-3, URL https://link.springer.com/book/10.1007/3-540-26404-3.

[7] S.G. Arutunian, K.G. Bakshetyan, N.M. Dobrovolsky, M.R. Mailian, L.A. Poghosyan, G. Sinenko, H.E. Soghoyan, I.E. Vasiniuk, K. Wittenburg, Petra proton beam profiling by vibrating wire scanner, in: 7th European Workshop on Beam Diagnostics and Instrumentation for Particle Accelerators, DIPAC 2005, 2005, pp. 181–183.

[8] J.T. Taylor, C. Waltham, T. Price, N.M. Allinson, P.P. Allport, G.L. Casse, A. Kacperek, S. Manger, N.A. Smith, I. Tsurin, A new silicon tracker for proton imaging and dosimetry, Nucl. Instrum. Methods Phys. Res. A 831 (2016) 362–366, http://dx.doi.org/10.1016/j.nima.2016.02.013.

[9] S. Levasseur, B. Dehning, S. Gibson, H. Sandberg, M. Sapinski, K. Sato, G. Schneider, J. Storey, Development of a rest gas ionisation profile monitor for the CERN Proton Synchrotron based on a Timepix3 pixel detector, J. Instrum. 12 (02) (2017) C02050.

[10] H. Blümer, C. Ebersberger, A scintillating fiber profile monitor for intense proton beams, Nucl. Instrum. Methods Phys. Res. A 365 (2–3) (1995) 268–272, http://dx.doi.org/10.1016/0168-9002(95)00513-7.

[11] C.O. Loch, M.A. Eichenberger, M. Togno, S.P. Zinsli, M. Egloff, A. Papa, R. Ischebeck, A.J. Lomax, P. Peier, S. Safai, Characterization of a low-cost plastic fiber array detector for proton beam dosimetry, Sensors (Switzerland) 20 (20) (2020) 1–13, http://dx.doi.org/10.3390/s20205727.

[12] S.H. Kim, J.W. Lee, W.S. Jung, J.K. Ahn, M.H. Jung, Y.J. Kim, Three-dimensional measurement of a proton beam profile at KOMAC with a scintillating fiber detector, Nucl. Instrum. Methods Phys. Res. A 1034 (2022) 166832.

[13] E. Rojatti, J. Bosser, M. Caldara, G. Calvi, M. Haguenauer, L. Lanzavecchia, A. Parravicini, P. Poilleux, M. Pullia, C. Viviani, Scintillating fibers used as profile monitors for the CNAO HEBT lines, in: 6th International Particle Accelerator Conference, 2015, p. MOPHA051, http://dx.doi.org/10.18429/JACoW-IPAC2015-MOPHA051.

[14] J. Wetzel, Y. Onel, B. Bilki, N. Bostan, O. Koseyan, E. Tiras, D. Winn, Radiation damage and recovery mechanisms in scintillating fibers, J. Phys. Conf. Ser. 2374 (1) (2022) 012121, http://dx.doi.org/10.1088/1742-6596/2374/1/012121.

[15] Scintillating fiber manufacturer website https://www.kuraray.com/products/psf.

[16] A. Mapelli, B. Gorini, M. Haguenauer, S. Jiguet, G. Lehmann Miotto, W. Vandelli, N. Vico Triviño, P. Renaud, Scintillation particle detection based on microfluidics, Sensors Actuators A 162 (1–3) (2010) 272–275, http://dx.doi.org/10.1016/j.sna.2010.03.040.

[17] A. Mapelli, B. Gorini, M. Haguenauer, S. Jiguet, N. Vico Triviño, P. Renaud, Novel radiation hard microfabricated scintillation detectors with high spatial resolution, Nucl. Instrum. Methods Phys. Res. A 617 (1–3) (2010) 400–401, http://dx.doi.org/10.1016/j.nima.2009.06.091.

[18] A. Mapelli, 'Scintillation Particle Detectors Based on Plastic Optical Fibres and Microfluidics (Ph.D. thesis), École Polytechnique Fédérale de Lausanne, Lausanne, 2011.

[19] P. Maoddi, A. Mapelli, P. Bagiacchi, B. Gorini, M. Haguenauer, G.L. Miotto, R.M. Garcia, F.S. Tehrani, S. Veneziano, P. Renaud, Scintillation detectors based on silicon microfluidic channels, J. Instrum. 9 (2014) C01019, http://dx.doi.org/10.1088/1748-0221/9/01/c01019.

[20] S. Flynn, S. Manolopoulos, V. Rompokos, A. Poynter, A. Toltz, L. Beck, L. Ballisat, J. Velthuis, P. Allport, S. Green, R. Thomas, T. Price, Monitoring pencil beam scanned proton radiotherapy using a large format CMOS detector, Nucl. Instrum. Methods Phys. Res. A 1033 (2022) 166703, http://dx.doi.org/10.1016/j.nima.2022.166703, URL https://www.sciencedirect.com/science/article/pii/S0168900222002443.

[21] A. Salehilashkajani, H.D. Zhang, M. Ady, N. Chritin, P. Forck, J. Glutting, O.R. Jones, R. Kersevan, N. Kumar, T. Lefevre, T. Marriott-Dodington, S. Mazzoni, I. Papazoglou, A. Rossi, G. Schneider, O. Sedlacek, S. Udrea, R. Veness, C.P. Welsch, A gas curtain beam profile monitor using beam induced fluorescence for high intensity charged particle beams, Appl. Phys. Lett. 120 (17) (2022) 174101.

[22] J. van de Walle, E. Forton, W. Kleeven, J. Mandrillon, V. Nuttens, E. Van Der Kraaij, Beam dynamics simulations of medical cyclotrons and beam transfer lines at IBA, in: 13th International Computational Accelerator Physics Conference, 2019, p. SUPAG09, http://dx.doi.org/10.18429/JACoW-ICAP2018-SUPAG09.

[23] F. Wang, B. Nachman, M. Garcia-Sciveres, Ultimate position resolution of pixel clusters with binary readout for particle tracking, Nucl. Instrum. Methods Phys. Res. A 899 (2018) 10–15.

[24] K.R. P. G. Pelfer, H.S. Rupprecht, Gallium Arsenide and Related Compounds-Proceedings of the 3rd International Workshop, World Scientific, 1996, p. 32, http://dx.doi.org/10.1142/9789814532297.

[25] S. Jan, G. Santin, D. Strul, S. Staelens, K. Assié, D. Autret, S. Avner, R. Barbier, M. Bardies, P. Bloomfield, et al., GATE: a simulation toolkit for PET and SPECT, Phys. Med. Biol. 49 (19) (2004) 4543.

[26] S. Jan, D. Benoit, E. Becheva, T. Carlier, F. Cassol, P. Descourt, T. Frisson, L. Grevillot, L. Guigues, L. Maigne, et al., GATE V6: a major enhancement of the GATE simulation platform enabling modelling of CT and radiotherapy, Phys. Med. Biol. 56 (4) (2011) 881.

[27] D. Sarrut, M. Bardiès, N. Boussion, N. Freud, S. Jan, J.-M. Létang, G. Loudos, L. Maigne, S. Marcatili, T. Mauxion, et al., A review of the use and potential of the GATE Monte Carlo simulation code for radiation therapy and dosimetry applications, Med. Phys. 41 (6Part1) (2014) 064301.

[28] D. Sarrut, M. Bała, M. Bardiès, J. Bert, M. Chauvin, K. Chatzipapas, M. Dupont, A. Etxebeste, L.M. Fanchon, S. Jan, et al., Advanced Monte Carlo simulations of emission tomography imaging systems with GATE, Phys. Med. Biol. 66 (10) (2021) 10TR03.

[29] S. Agostinelli, J. Allison, K.a. Amako, J. Apostolakis, H. Araujo, P. Arce, M. Asai, D. Axen, S. Banerjee, G. Barrand, et al., GEANT4—a simulation toolkit, Nucl. Instrum. Methods Phys. Res. A 506 (3) (2003) 250–303.

[30] C. Trigila, E. Roncali, Optimization of scintillator–reflector optical interfaces for the LUT Davis model, Med. Phys. 48 (9) (2021) 4883–4899.

[31] LUTDavismodel, 2022, https://github.com/OpenGATE/GateContrib/tree/master/imaging/LUTDavisModel (Accessed: 30-08-2022).

[32] H. Kolanoski, N. Wermes, Interactions of particles with matter, in: Particle Detectors, Oxford University PressOxford, 2020, pp. 23–88, http://dx.doi.org/10.1093/oso/9780198858362.003.0003.

[33] A. Mirandola, S. Molinelli, G. Vilches Freixas, A. Mairani, E. Gallio, D. Panizza, S. Russo, M. Ciocca, M. Donetti, G. Magro, S. Giordanengo, R. Orecchia, Dosimetric commissioning and quality assurance of scanned ion beams at the Italian National Center for Oncological Hadrontherapy, Med. Phys. 42 (9) (2015) 5287–5300, http://dx.doi.org/10.1118/1.4928397.

[34] G.R. Lynch, O.I. Dahl, Approximations to multiple Coulomb scattering, Nucl. Instrum. Methods Phys. Res. B 58 (1) (1991) 6–10, http://dx.doi.org/10.1016/0168-583X(91)95671-Y, URL https://www.sciencedirect.com/science/article/pii/0168583X9195671Y.